

Toward a Unified Model to Prevent Humping Defects in Gas Tungsten Arc Welding

The model can be used to help prevent humping when the effects of arc current, welding speed, shielding gas, electrode geometry, ambient pressure, torch angle, and external magnetic field are considered

BY A. KUMAR AND T. DEBROY

ABSTRACT. During gas tungsten arc (GTA) welding, high welding speed and current can lead to a serious weld defect with a bead-like appearance known as humping. Currently, there is no unified model to predict the formation of humping defects in GTA welding. Here we propose and test a new comprehensive computational model that can predict and prevent the formation of humping defects considering the values of arc current, welding speed, nature of the shielding gas, electrode geometry, ambient pressure, torch angle, and external magnetic field during gas tungsten arc (GTA) welding. The model considers stability of the waves on the weld pool surface due to relative motion between the shielding gas and the liquid metal based on the Kelvin-Helmholtz instability theory. The main factors for the instability were found to be the velocities of the shielding gas and the weld metal, densities of the molten metal and shielding gas, weld pool size, and surface tension of the molten weld metal. The weld pool size and weld metal velocities were calculated by a numerical heat transfer and fluid flow model, and the shielding gas velocity was calculated from an analytical relation. Good agreement between the model predictions of humping and the independent experimental results from various sources show that the model can be used to prevent humping considering the effects of arc current, welding speed, nature of the shielding gas, electrode geometry, ambient pressure, torch angle, and external magnetic field during GTA welding. Recommendations are provided for the use of special electrodes and an external magnetic field and, where practical, controlled pressure and careful selection of shielding gas to prevent humping under conditions when high welding speed and current are needed to sustain

A. KUMAR and T. DEBROY are with Department of Materials Science and Engineering, The Pennsylvania State University, University Park, Pa.

productivity goals.

Introduction

Productivity enhancement in the manufacturing of fabricated parts is often achieved by increasing welding speed and power. During arc welding, a continuous increase in the welding speed and current often results in a weld defect with bead-like appearance known as humping (Refs. 1–9). Various experimental investigations have been undertaken to understand and prevent humping. In addition, several theoretical models were proposed based on capillary instability (Refs. 1, 6), force balance, and scaling analysis (Refs. 7–9). The previous work on humping can be classified into three groups. First, efforts have been made to experimentally determine the onset of humping (Refs. 2, 3) during gas tungsten arc welding (GTAW). These results have provided an improved understanding of the effects of various variables on humping. Second, some of the previous modeling work (Refs. 1, 6) used Rayleigh's theory of instability of liquid metal cylinders to understand humping during welding. These efforts ignored important physical processes in welding and, therefore, the results are preliminary. Finally, force balance (Refs. 7–9) and nondimensional scaling analysis (Refs. 8, 9) were used to calculate conditions for humping. The nondimensional parameter-based calculations are accurate only within an order of magnitude. They are not designed to

explain the effects of all important welding variables and cannot precisely calculate the onset of humping. No comprehensive unified theoretical model exists today that can predict the formation of humping defects considering the effects of important welding variables such as the arc current, voltage, welding speed, nature of the shielding gas, electrode geometry, torch angle, and ambient pressure.

During GTA welding, a surface wave forms owing to the flow of shielding gas on the weld pool surface driven by a balance between molten metal's inertia, surface tension, and gravity forces (Refs. 10–12). The elevation and the velocity of the wave depend on various parameters such as the surface tension of liquid metal, densities of liquid metal and shielding gas, weld pool size, and the relative velocity between the shielding gas and the liquid metal. Any phenomenological model for understanding humping must take into account the effects of all the welding variables on the stability of the surface waves. An unstable surface wave can carry packets of liquid metals toward the solidifying region of the weld pool and contribute to humping.

Here we develop and extensively test a comprehensive mathematical model to quantitatively understand the welding conditions that result in humping defects. The model is based on Kelvin-Helmholtz hydrodynamic instability (Refs. 10–12) of waves on the surface of the weld pool. The model predicts humping when the elevation of the surface wave increases with time. Since the original Kelvin-Helmholtz model uses semi-infinite thickness of both the layers, a modified version is used here to take into account the finite depths of weld pools and specific thicknesses of the shielding gas layer depending on welding conditions. The velocity of the surface wave was determined by solving the potential flow equations with appropriate boundary conditions. The model indicates that the velocity of the surface wave is affected by

KEYWORDS

Gas Tungsten Arc Welding
Humping Defects
Kelvin-Helmholtz Hydrodynamic
Instability
Welding Speed
Welding Current

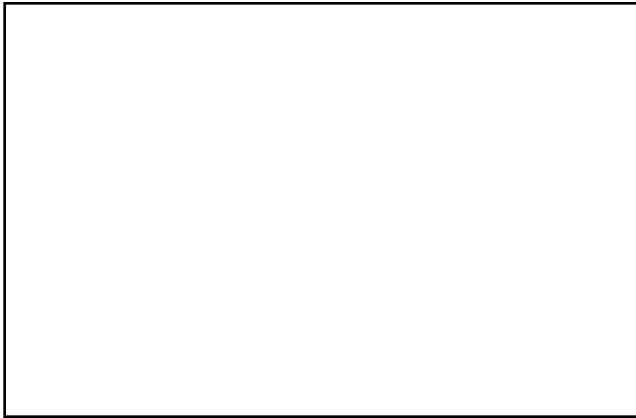


Fig. 1 — The waves generated at the interface of shielding gas layer and liquid metal in the weld pool due to shear across the interface.

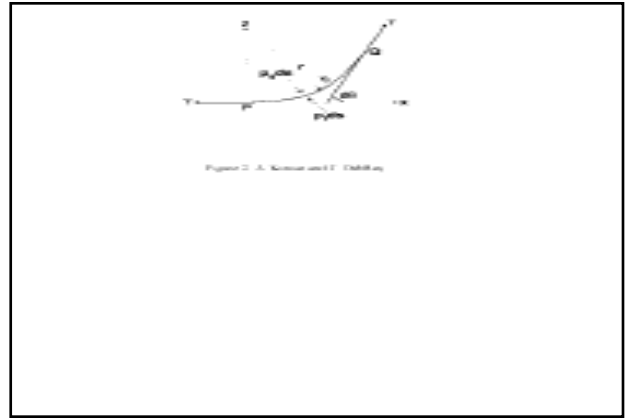


Fig. 2 — Segment of a free surface under the action of surface tension.

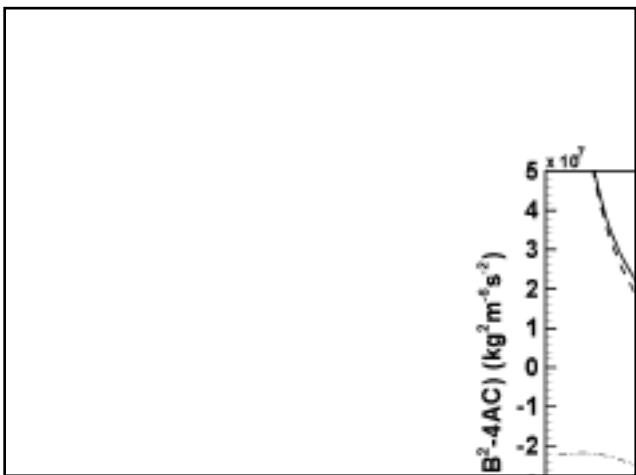


Fig. 3 — Effects of gravity and surface tension forces on the (B^2-4AC) term calculated by using Equations 16B–D and 17. The negative value of (B^2-4AC) term signifies the instability of surface wave or the initiation of humping in the weld pool. Values of different variables used in the calculation are: $h_l = 1.5$ mm, $h_g = 7.5$ mm, $U_l = 0.7$ m/s, $U_g = 210.0$ m/s, $\rho_l = 7200$ kg/m³, $\rho_g = 0.018$ kg/m³, and $\gamma = 1.8$ N/m. These values are selected because they represent the same order of the values in GTA welding with Ar shielding gas at 300 A, 11 mm/s welding speed, and arc length = 2.4 mm.

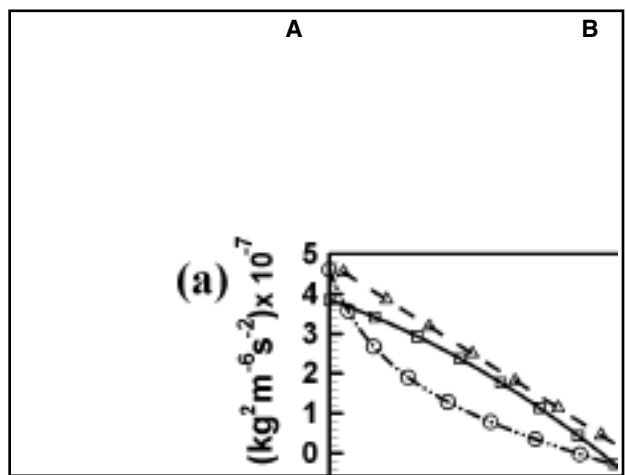


Fig. 4 — A — Sensitivity of U_g , ρ_g and L_p on (B^2-4AC) term given by Equations 16A–D; B — sensitivity of h_g , h_l , U_l , γ , and ρ_l on (B^2-4AC) term. The negative value of (B^2-4AC) term signifies the instability of the surface wave or the initiation of humping in the weld pool.

the surface tension of the liquid metal, densities of liquid metal and shielding gas, weld pool size, and the velocities of plasma and liquid metal on the weld pool surface. The weld pool size and liquid metal velocity were calculated by solving the equations of conservation of mass, momentum, and energy in three dimensions with appropriate boundary conditions (Refs. 13–21). The shielding gas velocity was calculated from an analytical relation of jet flow over a flat surface (Ref. 22). The computed results indicate how the values of arc current, welding speed, electrode tip angle, electrode type, nature of the shielding gas, ambient pressure, inclination of the torch, and the

external magnetic field affect humping formation in GTA steel welds. The computed welding conditions for the formation of humping were compared with the corresponding independent experimental results available in the literature for various GTA welding conditions. Recommendations are made to prevent humping under difficult conditions when high welding speed and current are needed to sustain productivity goals.

Background

Several researchers have proposed theories to predict humping. Based on the experiments on gas metal arc welding

(GMAW) of plain carbon steel in spray mode, Bradstreet (Ref. 1) suggested that humping occurs due to capillary instability. He applied Rayleigh's theory of instability of a free liquid cylinder and suggested the following expression:

$$L_c = 2\pi R \quad (1)$$

where L_c is the critical length of the weld pool and R is the radius of the cylindrical liquid metal that was claimed to represent the weld pool width. He suggested that when the length of the weld pool exceeds this critical length, L_c , humping occurs due to breakage of the cylindrical liquid metal and its premature solidifica-

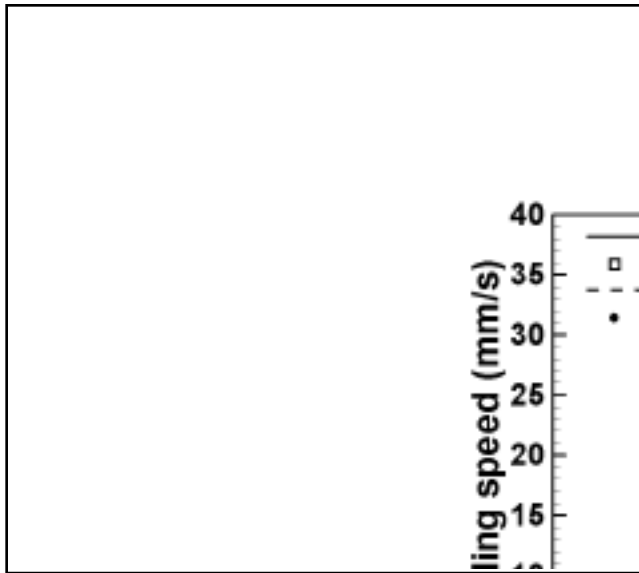


Fig. 5 — The variation of critical welding speed with arc current for argon and helium as shielding gases. The welding conditions used in the calculation are 2.4-mm arc length, 90-deg electrode tip angle, 3.2-mm-thick tungsten electrode, and the 1-atm ambient pressure. The welding speed higher than the critical speed will produce humping.

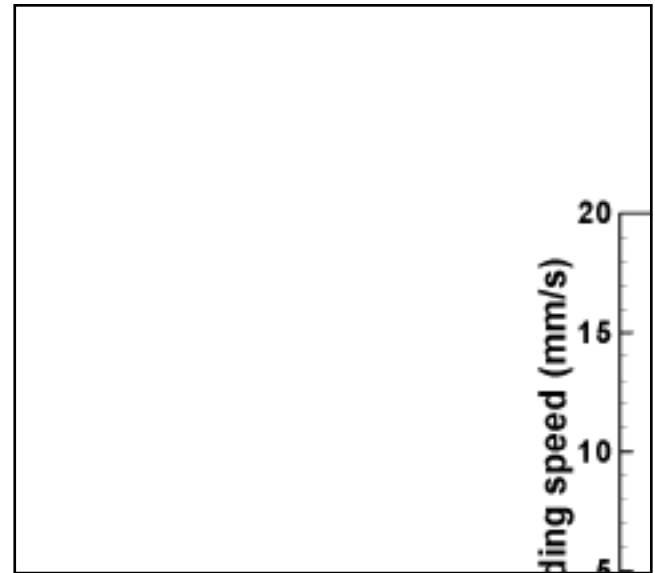


Fig. 6 — The effect of the electrode tip angle on humping. The welding conditions used in the calculations are 2.4-mm arc length, 3.2-mm-diameter tungsten electrode, argon shielding gas, and 1-atm. ambient pressure. The results show that the electrodes with smaller tip angle produce humping at a lower welding speed than those with larger tip angles.

Table 1 — Data Used for the Calculation of Weld Pool Geometry and the Velocity of the Liquid Metal by Three Dimensional Heat Transfer and Fluid Flow Model

Liquidus temperature (K)	1802
Solidus temperature (K)	1779
Density of liquid metal (kg m ⁻³)	7.87 x 10 ³
Viscosity of liquid (kg m ⁻¹ s ⁻¹)	6.3 x 10 ⁻³
Thermal conductivity of solid (J m ⁻¹ s ⁻¹ K ⁻¹)	36.4
Thermal conductivity of liquid (J m ⁻¹ s ⁻¹ K ⁻¹)	36.4
Specific heat of the solid (J kg ⁻¹ K ⁻¹)	754
Specific heat of the liquid (J kg ⁻¹ K ⁻¹)	805
Latent heat of melting (J kg ⁻¹)	2.7 X 10 ⁵
Temperature coefficient of surface tension (N m ⁻¹ K ⁻¹)	-0.47 X 10 ⁻³

Table 2 — Constants for Arc Characteristic Used In the Calculation of Arc Voltage (Refs. 25, 26)

Arc length (mm)	A	B	C
1.0	7.2	0.007	170
2.0	6.7	0.010	175
8.0	10.0	0.015	160
16.0	14.0	0.007	160

tion. Savage et al. (Ref. 2) experimentally determined the range of critical welding speed for humping in GTA welding for various welding conditions. Yamamoto and Shimada (Ref. 3) studied low-pressure GTA and suggested that the onset of humping was related to a transition in which the weld pool turns into a thin film under the arc and the metal velocity in the film exceeds a critical value depending on the thickness of the liquid

film. Beck et al. (Ref. 4) used a two-dimensional finite element model for calculating fluid flow in the molten pool during laser beam welding neglecting thermocapillary effects and observed that at high travel speeds, humping results from a jet created behind the keyhole. Mills and Keene (Ref. 5) proposed that humping was caused by Marangoni convection. In contrast, Gratzke et al. (Ref. 6) concluded that humping cannot be ex-

plained from Marangoni convection. They (Ref. 6) modified the model proposed by Bradstreet (Ref. 1) and calculated instability of a liquid cylinder based on Rayleigh's instability theory. The onset of humping was found to be influenced by the change in potential energy (due to capillarity) of a partially bounded liquid cylinder. The width of the weld pool was represented by the diameter of the cylinder and the weld pool length was taken as the length of the liquid cylinder.

$$L_c > 2\pi RB(\Phi_0) \quad (2A)$$

$$B(\Phi_0) = \left[1 - \left(\frac{\pi}{2(\pi - \Phi_0)} \right)^2 \right]^{-0.5} \quad (2B)$$

Equation 2A differs from Equation 1 by a function $B(\Phi_0)$. In Equation 2A, Φ_0 represents the half angle between the axis of the cylinder and the contact location of the cylinder with the workpiece (Ref. 6). Based on the shapes of typical arc and laser weld pools, Gratzke et al. (Ref. 6) suggested values of B as 1.5 and 2 for arc and laser beam welding, respectively. Thus, for arc welding, Equation 2A can be simplified to the following:

$$\frac{L_c}{R} = \frac{\text{Weld pool length}}{\text{Weld pool width}} > 3\pi \quad (3)$$

Apart from the simplification of the weld pool geometry, the gravitational and shear forces are ignored in Equations 1

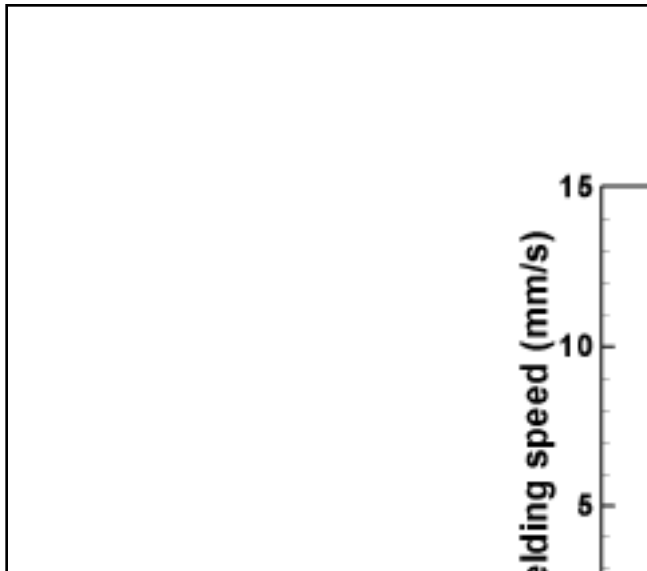


Fig. 7 — The effect of the hollow and solid electrodes on the critical welding speed to initiate humping. The welding conditions used in the calculation are 2.4-mm arc length, 90-deg electrode tip angle, argon shielding gas, and 1-atm. ambient pressure. The results show that solid electrodes produce humping at lower welding speeds than hollow electrodes.



Fig. 8 — The effect of the externally applied transverse magnetic field on arc deflection based on Fleming's left-hand rule. The arc is deflected in the welding direction when the north pole is on the left side of the moving electrode. If the north and south poles are interchanged, the arc will be deflected in the reverse direction.

and 3, and they cannot predict the conditions for the initiation of humping.

Yamauchi and Taka (Ref. 7) compared the arc and the metalostatic pressures at the tail of the weld pool to explain humping. Mendez and Eagar (Ref. 8) and Mendez et al. (Ref. 9) explained the periodic nature of humping by finding the location of the transition line between the arc gouge and the trailing region based on pressure balance. Their model was based on scaling laws, and they predicted humping at high arc currents (Refs. 8, 9).

Mathematical Model

Humping Model Based on Kelvin-Helmholtz Hydrodynamic Instability

The following simplifying assumptions were made.

a) The motion of the surface waves along the direction of welding is considered in the model.

b) The liquid is assumed to be incompressible and inviscous for the calculation of the surface wave velocity for simplicity.

c) The shielding gas flow is assumed to be steady and specified by a constant horizontal velocity.

On the weld pool surface, the wave propagation is represented by the following wave equation:

$$\frac{\partial^2 \eta}{\partial x^2} = \frac{1}{c^2} \frac{\partial^2 \eta}{\partial t^2} \quad (4)$$

Table 3 — Effect of Various Welding Variables on the Parameters Required to Predict the Humping Defects

Welding variable	Parameters affected
Arc current	Depth of weld pool, velocity of liquid metal, length of the pool, surface tension of the liquid metal, velocity of arc plasma
Arc length	Depth of weld pool, velocity of liquid metal, length of the pool, surface tension of the liquid metal, velocity of arc plasma, height of shielding gas layer
Nature of the shielding gas	Depth of weld pool, velocity of liquid metal, length of the pool, surface tension of the liquid metal, velocity of arc plasma, density of the gas
Nozzle to workpiece distance	Height of shielding gas layer
Electrode tip angle	Depth of weld pool, velocity of liquid metal, length of the pool, surface tension of the liquid metal, velocity of arc plasma
Ambient pressure	Depth of weld pool, velocity of liquid metal, length of the pool, surface tension of the liquid metal, velocity of arc plasma
Electrode inclination angle	Depth of weld pool, velocity of liquid metal, length of the pool, surface tension of the liquid metal, velocity of arc plasma

Table 4 — Values of Effective Arc Radius, r_j , for Current Density Distribution, and Effective Arc Radius for Heat Flux Distribution, r_q , in mm for Different Welding Conditions (Refs. 25, 27, 31–35) Used in the Heat Transfer and Fluid Flow Calculations and Arc Velocity Calculation (Ref. 22). The Variables I and I_a in the Table Represent Arc Current (A) and Arc Length (mm), Respectively

Argon shielding gas, 1 atm. pressure, 90-deg electrode tip angle	$r_j = 1.085 \times I^{0.2892}$ $r_q = 7.543 \times I^{0.2645} I_a^{0.3214}$
Argon shielding gas, 1 atm. pressure, 18-deg electrode tip angle	$r_j = 1.017 \times I^{0.2892}$ $r_q = 6.786 \times I^{0.2645} I_a^{0.3214}$
Argon shielding gas, 32 mm Hg pressure, 25-deg electrode tip angle	$r_j = 10.67 \times I^{0.2892}$ $r_q = 7.466 \times I^{0.2645} I_a^{0.3214}$
Helium shielding gas, 1 atm. pressure, 90-deg electrode tip angle	$r_j = 1.391 \times I^{0.2892}$ $r_q = 9.666 \times I^{0.2645} I_a^{0.3214}$

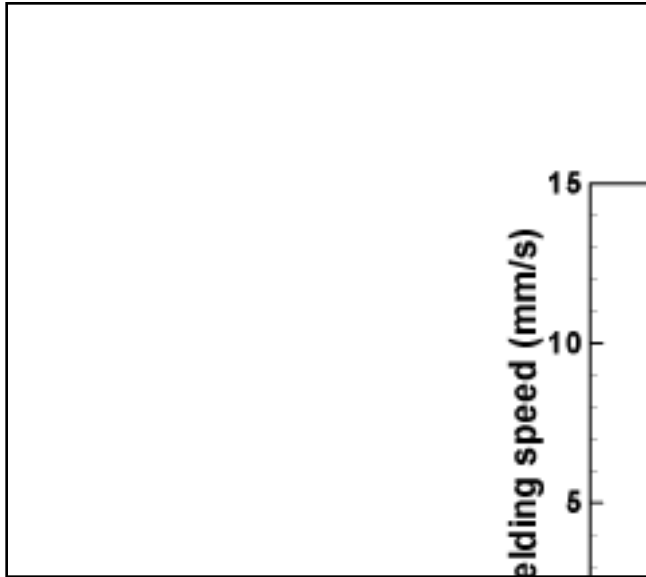


Fig. 9 — The effect of the externally applied transverse magnetic field on the critical welding speed to initiate humping in the weld. The welding conditions used in the calculation are 2.4-mm arc length, 90-deg electrode tip angle, argon shielding gas, and 1-atm. ambient pressure. The results show that the critical welding speed increases with the increase in externally applied transverse magnetic field.

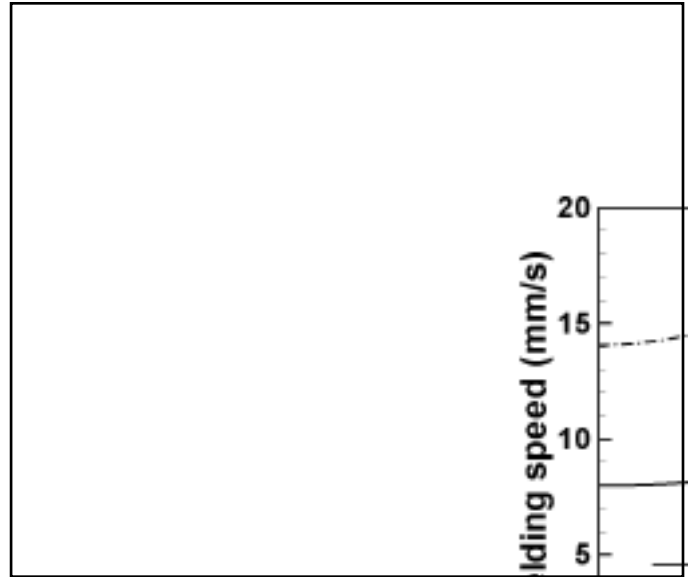


Fig. 10 — The variation of critical welding speed with externally applied transverse magnetic field for different arc lengths. The welding conditions used in the calculation are 300-A arc current, 90-deg electrode tip angle, argon shielding gas, and the 1-atm. ambient pressure. The results show that the critical welding speed increases with the increase in externally applied transverse magnetic field and the arc length.

where η is local elevation that depends on position along the welding direction, x , and time, t , and c is the velocity of the wave opposite to the welding direction x . Equation 4 represents the motion of the wave on the weld pool surface in the x direction since it is assumed that the wave is traveling along the welding direction, and there is no significant motion in the y direction. This assumption is made

based on the fact that humping defects appear mainly along the welding direction. The general solution of Equation 4 is given by the following expression (Ref. 10):

$$\eta = ae^{ik(x-ct)} \quad (5)$$

where a is the amplitude and k is the wave number. The wave speed, c , can be expressed in general form as follows:

$$c = \alpha + i\beta \quad (6)$$

where α and β are the real and the imaginary parts of the wave speed, respectively. After substituting the expression for c in Equation 5, we get the following:

$$\eta = ae^{ik(x-[\alpha + i\beta]t)} = ae^{ik(x-\alpha t)}e^{-k\beta t} \quad (7)$$

Equation 7 shows that if β is positive, the value of elevation, η , will increase with time and the interface between the liquid metal and shielding gas will become unstable. It should be noted that η cannot be determined from Equation 7 unless the values of α and β that characterize the wave velocity are known. In order to determine the stability of the surface wave, its velocity given by Equation 6 needs to be calculated. The velocity of the wave depends on shape of the weld pool surface in the x - z plane and can be calculated by solving the velocity potentials in the gas and the liquid phases from the following two Laplace equations (Refs. 10–12):

$$\frac{\partial^2 \Phi_1}{\partial x^2} + \frac{\partial^2 \Phi_1}{\partial z^2} = 0 \quad (8A)$$

Table 5 — Properties of Shielding Gas (Refs. 22, 25, 33, 35) Required for Arc Velocity Calculation Using the Expression Proposed by Chang Et Al. (Ref. 22)

At 1 atmospheric pressure (i.e. 760 mm Hg pressure)	Density of argon gas	0.018 kg/m ³
	Viscosity of argon gas	2.32 x 10 ⁻⁴ kg. m ⁻¹ sec ⁻¹
	Cathode radius	1.191 x 10 ⁻³ m
	Density of helium gas	0.0018 kg/m ³
At 32 mm Hg pressure	Viscosity of helium gas	4.32 x 10 ⁻⁴ kg ⁻¹ sec ⁻¹
	Density of argon gas	0.0018 kg/m ³
	Viscosity of argon gas	1.90 x 10 ⁻⁴ kg. m ⁻¹ sec ⁻¹
	Cathode radius	1.19 x 10 ⁻³ m

Table 6 — Welding Conditions of Mendez and Eagar (Ref. 8) Used for the Prediction of Humping by the Proposed Model

Arc current (A)	Welding speed (mm/s)	Arc length (mm)	Sulfur content (ppm)	Humping
274	11.6	7.3	6	No
334	14.1	7.5	6	No
500	10.6	9.4	6	No
500	15.0	8.5	6	No
500	10.6	9.2	230	Yes
500	15.0	8.2	230	Yes

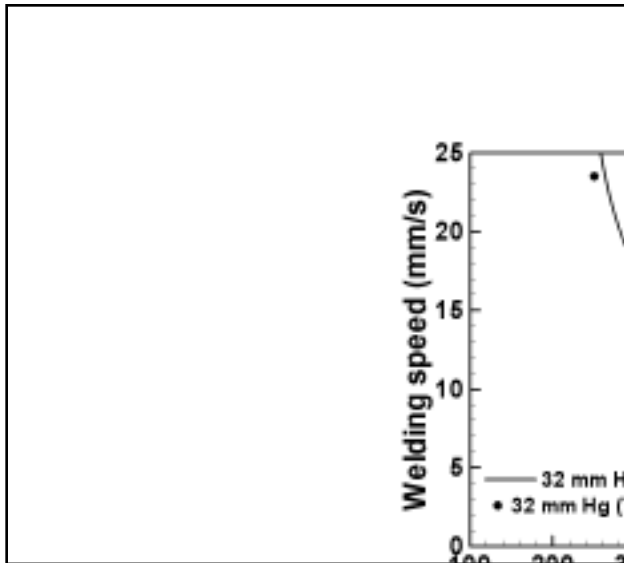


Fig. 11 — The variation of critical welding speed with arc current at low pressure for vertical torch position. The welding conditions used in the calculation are 2.4-mm arc length, 25-deg electrode tip angle, 3.2-mm-diameter tungsten electrode, argon shielding gas, and 32 mm of Hg ambient pressure. Higher values of critical welding speed were achieved at low ambient pressures.

$$\frac{\partial^2 \Phi_g}{\partial x^2} + \frac{\partial^2 \Phi_l}{\partial z^2} = 0 \quad (8B)$$

where x is the direction opposite to the welding direction, z is the vertical direction, and Φ_l and Φ_g are the velocity potentials in the liquid metal and shielding gas, respectively. These velocity potentials (i.e., Φ_l and Φ_g) are the functions of wave speed, c , and need to be calculated using appropriate boundary conditions. The welding torch position is selected as the origin of Cartesian coordinate system to simplify the solution of governing Laplace equations. It should be noted that we need four sets of boundary conditions in each layer to solve the velocity potentials defined by Equations 8A and B. The first set of boundary conditions can be written using the known velocities of the liquid metal (U_l) and shielding gas (U_g) as follows:

$$\frac{\partial \Phi_l}{\partial x} = U_l \quad (9A)$$

$$\frac{\partial \Phi_g}{\partial x} = U_g \quad (9B)$$

The liquid metal velocity, U_l , was calculated from three-dimensional heat transfer and fluid flow calculations while the shielding gas velocity, U_g , was calculated

using the analytical expressions as explained in the next section. The velocities of the liquid and gas at the surface depend on the location on the surface. The calculations were performed with maximum velocities on the weld pool surface to ensure consideration of the location most susceptible to humping. The second set of boundary conditions can be written by linking the velocity potentials with the local elevation position function through the following expression (Refs. 10–12):

$$\frac{D\eta}{Dt} = \left(\frac{\partial \Phi_l}{\partial z} \right)_{z=\eta} = \left(\frac{\partial \Phi_g}{\partial z} \right)_{z=\eta} \quad (10)$$

$$\text{where } \frac{D}{Dt} = \frac{\partial}{\partial t} + U \frac{\partial}{\partial x}$$

Equation 10 represents that the substantial derivative of the surface position function of the wave, η , is equal to the normal velocity of the fluids at the interface since the fluid particles at the interface move with the surface wave. After expanding the

$$\left(\frac{\partial \Phi_l}{\partial z} \right)_{z=\eta} \quad \text{and} \quad \left(\frac{\partial \Phi_g}{\partial z} \right)_{z=\eta}$$

using Taylor's theorem and neglecting the higher-order terms, the following expressions are obtained for both the liquid and gas layers (Refs. 10–12):

$$\frac{\partial \eta}{\partial t} + U_l \frac{\partial \eta}{\partial x} = \left(\frac{\partial \Phi_l}{\partial z} \right)_{z=0} \quad (11A)$$

$$\frac{\partial \eta}{\partial t} + U_g \frac{\partial \eta}{\partial x} = \left(\frac{\partial \Phi_g}{\partial z} \right)_{z=0} \quad (11B)$$

where $z = 0$ is the interface between the shielding gas layer and liquid metal as shown in Fig. 1. The first and second terms on the left-hand side in Equations 11A and B represent the local rate of change of surface wave profile at a given point and convective term due to change in η as a result of flow of the fluids. The third set of boundary conditions is written based on the assumption made earlier that there is no net flow across the shielding gas and liquid metal layer along the vertical direction as follows:

$$\left(\frac{\partial \Phi_l}{\partial z} \right)_{z=-h_1} = 0 \quad (12A)$$

$$\left(\frac{\partial \Phi_g}{\partial z} \right)_{z=h_g} = 0 \quad (12B)$$

where h_1 is the depth of the weld pool, and h_g is the height of the shielding gas layer as shown in Fig. 1. The fourth and the final set of boundary conditions is written based on pressure and energy balance using the unsteady Bernoulli's theorem to keep the pressure continuous at the interface. These boundary conditions in each layer are (Refs. 10–12) as follows:

$$P_l + \rho_l \left[\frac{\partial \Phi_l}{\partial t} + \frac{1}{2} \left\{ \left(\frac{\partial \Phi_l}{\partial x} \right)^2 + \left(\frac{\partial \Phi_l}{\partial z} \right)^2 \right\} \right] + g\eta = \text{constant} \quad (13A)$$

$$P_g + \rho_g \left[\frac{\partial \Phi_g}{\partial t} + \frac{1}{2} \left\{ \left(\frac{\partial \Phi_g}{\partial x} \right)^2 + \left(\frac{\partial \Phi_g}{\partial z} \right)^2 \right\} \right] + g\eta = \text{constant} \quad (13B)$$

where ρ_l and ρ_g are the densities of liquid metal and shielding gas, respectively, P_l and P_g are the pressures in lower liquid and upper gaseous layers, respectively, and g is the acceleration due to gravity. The first, second, third, and fourth terms

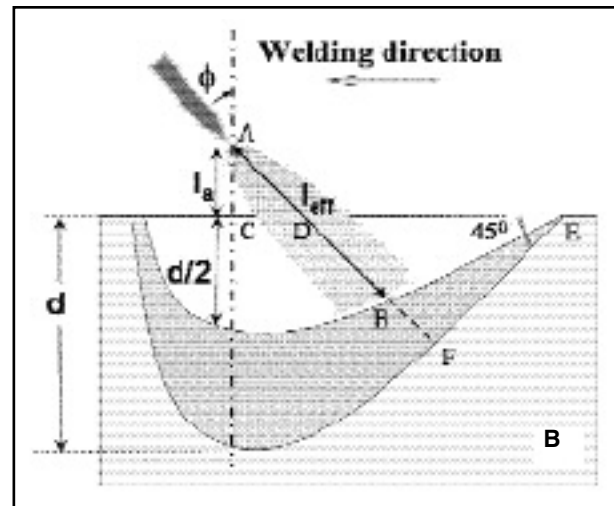
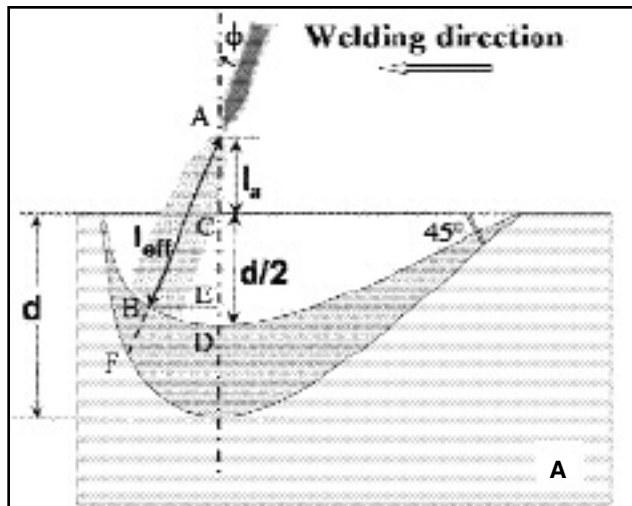


Fig. 12 — The effect of torch inclination on the effective arc length. A — The welding torch in push position; B — the pull position.

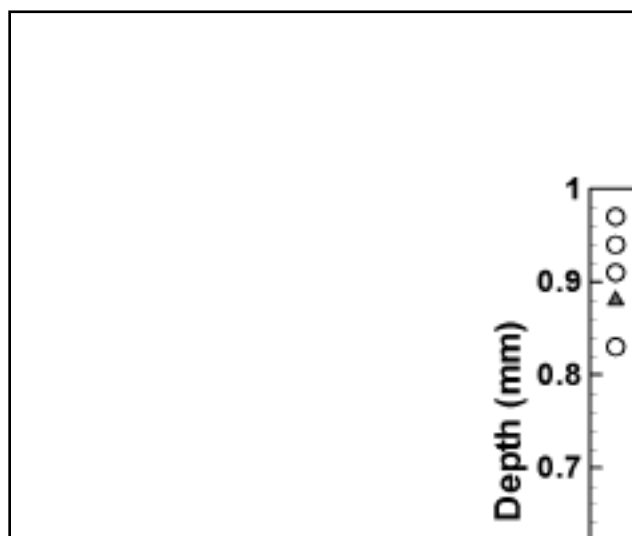


Fig. 13 — The variation of weld pool depth with inclination of torch for 67.0-A arc current, 9.0 arc voltage, and 4.0 mm/s welding speed. The positive torch angle means that the welding torch is in push position while the negative angle means that the torch is used in the pull position.

on the left-hand side of Equations 13A and B represent the pressure, unsteady velocity potential, kinetic energy, and potential energy terms, respectively (Ref. 10). The effect of surface tension was calculated by considering a force balance on the free liquid pool surface as shown in Fig. 2. The pressure difference at the interface due to surface tension can be written as follows:

$$P_g - P_1 = \gamma \frac{\partial^2 \eta}{\partial x^2} \quad (14)$$

where γ is the surface tension of the liq-

uid weld metal. Equation 14 was obtained by balancing forces in a direction perpendicular to an arc segment PQ of the free surface as explained in Appendix A. The final expressions of velocity potentials obtained after solving Equations 8A and B using the boundary conditions given by Equations 9–14 are the values of local elevation, η , as a function of time, t . After subtracting Equation 13A from 13B and substituting the values of velocity potentials, the following relation was obtained as derived in Appendix A:

$$\coth(h_g k) = \gamma k^2 + g(\rho_1 - \rho_g) \quad (15)$$

Equation 15 provides the velocity of surface wave traveling opposite to the welding direction (Refs. 10–12). The velocity of the traveling wave is given by

$$c = \alpha + i\beta = \frac{-B + \sqrt{B^2 - 4AC}}{2A} \quad (16A)$$

$$\text{where } A = -k \begin{pmatrix} \rho_1 \coth(h_1 k) \\ + \rho_g \coth(h_g k) \end{pmatrix} \quad (16B)$$

$$B = 2k \begin{pmatrix} U_1 \rho_1 \coth(h_1 k) \\ + U_g \rho_g \coth(h_g k) \end{pmatrix} \quad (16C)$$

$$C = \gamma k^2 + g(\rho_1 - \rho_g) - k \begin{pmatrix} U_1^2 \rho_1 \coth(h_1 k) \\ + U_g^2 \rho_g \coth(h_g k) \end{pmatrix} \quad (16D)$$

A three-dimensional heat transfer and fluid flow model described in the next section was used to calculate the length, L_p , the depth, h_1 , and the surface velocity, U_1 , of the weld pool. The wave number, k , is $2\pi/L$ where L is the length scale that is taken as the length of the weld pool, L_p :

$$k = \frac{2\pi}{L_p} \quad (17)$$

Equation 16A shows that the velocity of the wave can be real or complex depending on the value of term $(B^2 - 4AC)$. If this term is negative and, consequently, β is positive, the instability will grow in the weld pool because value of elevation, η , will increase with time as indicated in Equation 7.

Three-Dimensional Heat Transfer and Fluid Flow Model

The equations of conservation of mass, momentum, and energy are solved

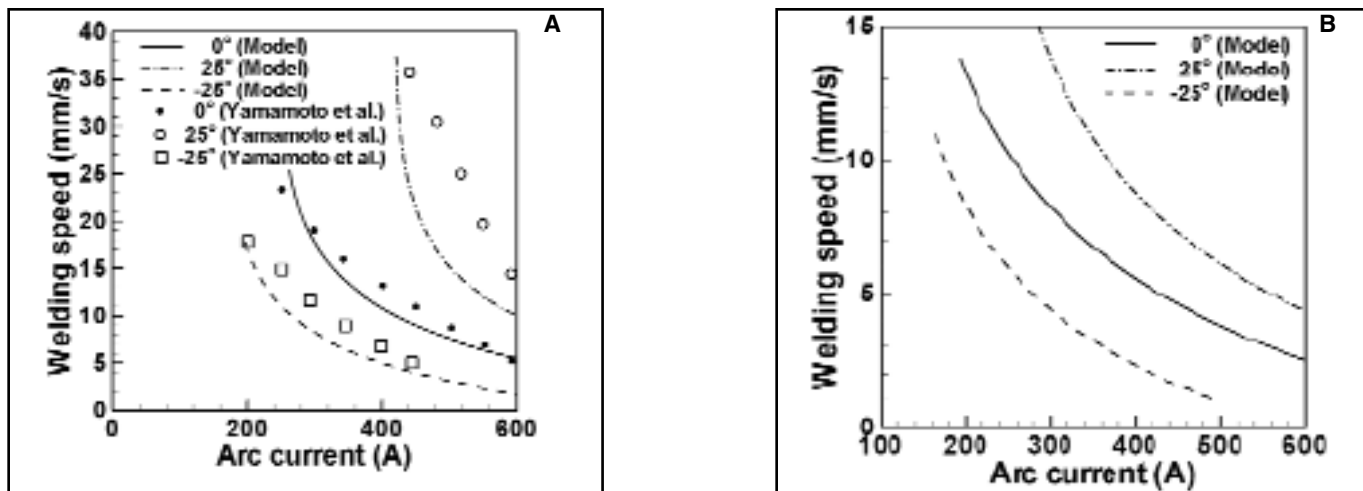


Fig. 14 — The variation of critical welding speed with arc current for the initiation of humping defects in the weld for different torch angles at the following: A — Atmospheric pressure; B — at 32-mm Hg pressure. Higher values of critical welding speed were achieved when the welding torch was in the push configuration, i.e., when the arc strikes ahead of the torch axis.

numerically in three-dimensional Cartesian coordinate system (Refs. 13–21) to obtain the values of weld pool length, liquid metal velocity, and the peak temperature. Two-dimensional calculations of heat transfer and fluid flow can also be performed to calculate the values of these variables. The governing equations and the boundary conditions used to calculate the temperature and velocity profiles and the weld pool geometry are explained in Appendix B. The governing equations are discretized using the control volume approach based on the power law scheme (Ref. 23). At each time step, the discretized equations are solved using the widely used SIMPLE algorithm (Ref. 23). Fine, nonuniform grids with finer grid spacing near the heat source were used to achieve high computational accuracy. A typical grid system contained $101 \times 61 \times 41$ grid points in a 8-cm long, 5-cm wide, and 2-cm deep computational domain. The minimum grid spacing along the x, y, and z directions were about 200, 200, and 125 μm , respectively.

The surface tension of the molten steel (γ) in the weld pool was calculated by using the following expression (Ref. 24):

$$\gamma = 1.943 - 4.3 \times 10^{-4}(T - 1809) - 1.3 \times 10^{-8}RT \cdot \ln [1 + 0.00318a_s e^{(1.66 \times 106/RT)}] \quad (18)$$

where T is the average of liquidus temperature and peak temperature of the liquid metal in the weld pool in K, R is the universal gas constant, and a_s is the activity of the sulfur in steel. The material properties used in the heat transfer and fluid flow calculations are listed in

Table 1. The liquid metal velocity, U_l , is taken as the peak velocity present on the weld pool surface. The arc voltage (V) required for the calculation of input power at any current level for constant arc length was calculated by using the following volt-ampere characteristic expression:

$$V = A + B \times I + C/I \quad (19)$$

where A, B, and C are the constants whose values are available in the literature (Refs. 25, 26) and listed in Table 2.

Average Velocity and Other Arc Parameters

During GTA welding, the Lorentz force creates a pressure difference between the anode (workpiece) and the cathode (electrode). Due to high current density near the electrode compared to the workpiece surface, the static pressure at the cathode was higher than the anode. This pressure difference produces a jet of plasma toward the anode. In GTAW, the arc pressure is caused by the momentum transfer of the impinging plasma jet on the weld pool and is a major factor in producing surface depressions and weld defects (Refs. 8, 9). The dependence of arc pressure (p_{arc}) on the arc velocity (V_{arc}) could be expressed as follows (Refs. 25, 27):

$$p_{arc} = \frac{1}{2} \rho_g V_{arc}^2 \quad (20)$$

The arc velocity depends on the welding current, arc length, electrode shape, and the shielding gas composition, and was calculated using the expressions pro-

posed by Chang et al. (Ref. 22).

The current density distribution required for the calculation of arc velocity was assumed to be Gaussian and could be described by the following function (Refs. 28, 29):

$$J = \frac{3I}{\pi r_j^2} \exp\left(-\frac{3r^2}{r_j^2}\right) \quad (21)$$

where J is the current density, I is current, r is the radial distance from the arc location, and r_j is the effective radius of the arc. Using Equation 21, the maximum and average current density could be written as (Refs. 25, 27) the following:

$$J_{max} = \frac{3I}{\pi r_j^2} \quad (22)$$

$$J_{avg} = \frac{I}{\pi r_j^2} = \frac{1}{3}(J)_{max} \quad (23)$$

Lin and Eagar (Ref. 27) suggested that current density is proportional to arc velocity based on the following relation:

$$p_{arc} = \frac{1}{2} \rho_g V_{arc}^2 = \frac{\mu_o J_{avg}^2 r_j^2}{4} \quad (24)$$

where μ_o is the magnetic permeability of free space. Using Equations 22–24, we can write

$$U_g = (V_{arc})_{avg} = \frac{1}{3}(V_{arc})_{max} \quad (25)$$

where $(V_{arc})_{max}$ is the maximum value of arc velocity (i.e., at $r = 0$) along the arc axis.

At high arc pressures, the weld pool

surface gets deformed and the distance between the electrode and the workpiece increases (Ref. 30). Therefore, the following expression of effective arc length (l_{eff}) was used to calculate the maximum arc velocity (Ref. 8):

$$l_{eff} = \text{arc length} + 0.5 \times \text{depth of weld pool} \\ \text{pool} = l_a + 0.5 \times h_l \quad (26)$$

Results and Discussion

Sensitivity of Different Variables on Humping

The effects of various welding variables on the parameters that affect humping are listed in Table 3. It can be seen from this table that almost all of the welding variables affect the depth and length of the weld pool, liquid metal velocity in the weld pool, surface tension of the liquid metal, and the velocity of the arc jet. The values of these variables also affect the velocity of the surface wave given by Equation 15, which includes the effects of surface tension, shear force, pressure gradient, and gravity.

Figure 3 shows the effects of ignoring either the gravity or the surface tension effect on the humping formation based on the value of (B^2-4AC) . The values of A, B, and C are calculated from Equations 16B-D, and the data indicated in the caption of Fig. 3. If the effect of the gravity in the instability criteria given by is neglected, the (B^2-4AC) term is positive only for smaller weld pool length and the model will predict humping even for the safe welding conditions. The results indicate that the gravitational force has a significant stabilizing effect that cannot be ignored. On the other hand, if the surface tension effect is neglected, the weld pool is unstable under all welding conditions. So consideration of both the surface tension and gravity effects are necessary to accurately predict humping.

Figure 4A, B shows the sensitivity of various variables such as U_g , ρ_g , L_p , U_b , h_g , h_l , ρ_l , and γ , on the value of the (B^2-4AC) term. Higher values of U_g , ρ_g , and L_p decreases the value of (B^2-4AC) , making the weld pool more susceptible to humping due to higher drag force as shown in Fig. 4A. Figure 4B shows that the liquid weld metal with high surface tension (i.e., low percentage of sulfur and relatively lower temperature) is more stable than a liquid metal with low surface tension. The increase in γ enhances the resistive power of the liquid metal against the drag force. Furthermore, the prominent effect of increase of γ on humping can be observed from the steep slope of (B^2-4AC) vs. γ plot in Fig. 4B. On the other hand, the increase in the

values of h_g , h_l , U_b , and ρ_l have a significantly mild effect on the value of the (B^2-4AC) term as can be seen from the relatively low slopes of plots in Fig. 4B. The relatively mild effect of U_b on the value of the (B^2-4AC) term justifies the use of the peak surface velocity in the calculations.

Effect of Arc Current and Welding Speed

The length of the weld pool and the arc velocity significantly affects humping. The effective arc radius used for the calculation of the depth and length of the weld pool from heat transfer and fluid flow calculations are listed in Table 4. The properties of shielding gas used for calculating the arc velocity are given in Table 5 for different welding conditions. For each combination of arc current and welding speed, values of U_b , U_g , ρ_b , ρ_g , h_l , h_g , L_p , and γ were substituted in Equation 16A to calculate the value of (B^2-4AC) . The calculated line in Fig. 5 represents zero value of the (B^2-4AC) . The region above this line has a negative value of (B^2-4AC) ; as a result, humping defects appear for those welding conditions.

With the increase in arc current, both the temperature in the weld pool and the arc velocity increase. The high arc velocity increases the viscous drag force on the weld pool surface and decreases the (B^2-4AC) term. The higher current also increases the temperature in the weld pool, which decreases the surface tension of the liquid metal. Figure 5 shows that humping may occur due to decreased surface tension and increased drag force at high currents even at low welding speeds.

When the current is kept constant, the depth of the weld pool decreases with the increase in the welding speed. The lower weld pool depth decreases the effective arc length and increases the arc velocity. Thus, the higher welding velocity increases the drag force and makes humping more likely as shown in Fig. 5. Calculations were done for the conditions similar to those chosen by Savage et al. (Ref. 2) in their experiments. In particular, argon shielding gas, the electrode-to-workpiece distance of 2.4 mm, electrode thickness of 3.2 mm, and vertex angle of 90 deg were considered. Humping would occur if the welding speed is higher than the critical speed in Fig. 5 for the welding conditions considered as can be observed from both experimental data and the calculations. Table 6 also shows a good agreement in predicting humping for a different set of experiments conducted by Mendez et al. (Ref. 8). Good agreement between the calculated and

the experimentally obtained critical speed limits (Refs. 2, 8) shows that the model can satisfactorily predict humping for a wide variety of welding conditions.

Effect of Shielding Gas

Since the nature of the shielding gas affects arc shape (Refs. 25, 27, 31, 32), it also influences the current density distribution. The arc shape influences the pressure difference between the cathode and the anode and, therefore, the arc pressure. According to Lin and Eagar (Ref. 27), the spread of the plasma or the effective current radius is proportional to η^2/ρ , where η is the viscosity and ρ is the density of the gas. Since the density and viscosity of helium was about 1/10th and twice, respectively, those of argon, at high temperatures (Refs. 27, 33), the helium arc is broader than that of argon. Savage et al. (Ref. 2) also reported that the argon arc was brighter and more cylindrical than the helium arc. The density and viscosity of helium used in the calculations are listed in Table 5.

The arc velocity is lower in He than in Ar due to the low density and high viscosity of helium. As a result, the drag force of He on the liquid metal is lower than that of Ar. The critical welding speed for humping was higher by a factor of 3 in helium than in argon for the same values of arc current and voltage as shown in Fig. 5. Comparisons of the results for He and Ar show that in He humping does not occur at low arc currents even at high welding speeds. Use of Ar makes welds more susceptible to humping. The computed critical welding speed for humping shows good agreement with the corresponding experimental values reported in the literature (Ref. 2).

Effect of the Electrode Tip Angle

Several researchers (Refs. 24, 26, 31, 32, 34, 35) have shown that the electrode tip angle significantly affects arc behavior. Tsai and Eagar (Ref. 31) found that the arc radius increased by approximately 15% when the current increased from 100 to 200 amps in Ar-plasma with a 75-deg tip angle and 5.5-mm arc length. Yamauchi and Taka (Ref. 32) have shown that the effect of electrode tip angle on arc pressure was more pronounced at high current levels. Lin and Eagar (Ref. 27) observed that the arc pressure increased when electrodes with sharper tip angles were used. With an increase in arc pressure for sharper tip electrodes (e.g., 18-deg tip), the peak current density and arc velocity also increases. As a result, the drag force on the liquid metal increases, which makes humping more

likely as shown in Fig. 6. The experimental values of critical welding speed for humping reported by Savage et al. (Ref. 2) and Yamamoto and Shimada (Ref. 3) for 18-, 25-, and 90-deg electrode tip angles show a good agreement with the corresponding computed values. Therefore, electrodes with a large tip angle can be used to achieve high welding speed and prevent humping.

Effect of Electrode Shape

Yamauchi and Taka (Ref. 32) showed that the use of hollow electrodes in place of solid electrodes reduced the arc force. They (Ref. 32) found that the arc root formed symmetrically inside the hole for a typical 5-mm-diameter tungsten electrode with a 3-mm central hole. They suggested that the average arc velocity reduced by about 15% compared to a solid electrode based on the measurement of arc force by Yamauchi and Taka (Ref. 32). The decrease in the arc velocity reduced the drag force on the liquid metal and increased the computed critical welding speed for humping by about 50% as shown in Fig. 7. The computed results are consistent with the fact that the hollow electrodes reduce the arc pressure (Ref. 36) and, therefore, they may be used to achieve a high fabrication rate and prevent humping under welding conditions where humping may occur when solid electrodes are used.

Effect of External Magnetic Field

An external magnetic field applied transverse to the welding direction will deflect the arc due to electromagnetic force. Depending on the direction of the field, a transverse magnetic field will deflect the arc either in the welding direction or opposite to it (Refs. 25, 37, 38) as shown in Fig. 8. The deflection of the arc increases the effective arc length and arc radius. The increase in arc length decreases the arc velocity and drag force on the weld pool surface.

The extent of the arc deflection (δ) depends linearly on the magnitude of the externally applied magnetic field and the effective arc length (l_{eff}) as represented by the following equation (Refs. 24, 37, 38):

$$\delta = K_1 B_x l_{eff} \quad (27)$$

where K_1 is a constant and B_x is the externally applied magnetic field in Tesla. The value of constant, K_1 , was obtained to be 100.0 Tesla^{-1} by fitting the above equation with the experimental results reported in the literature (Ref. 37) for Ar shielding gas. However, the value of the constant, K_1 , may vary with welding conditions like welding current, shielding gas

composition, and the ambient pressure. The modified effective arc length (l_{eff}) could be calculated by using the value of arc deflection (δ) as follows:

$$l_{eff} = \sqrt{\delta^2 + \left(\text{arc length} + 0.5 \times \text{depth of weld pool} \right)^2} \quad (28)$$

The higher effective arc length decreased the magnitude of the drag force created by the flow of the plasma on the liquid metal in the weld pool. The reduction in drag force with increase in the magnitude of the external magnetic field reduced the chances of humping in the weld and increased the critical welding speed by 10–15% for magnetic field of 0.003 Tesla as shown in Fig. 9. Furthermore, the critical welding speed increases by more than 75% when the arc length increases from 2.4 to 3.0 mm as shown in Fig. 10. The computed results show that the longer arc length and an appropriate transverse external magnetic field during welding would provide a higher operating welding speed without any humping.

Effect of Ambient Pressure

Higher ambient pressure increases the current density in the arc column (Refs. 3, 25, 39, 40). Matsunawa and Nishiguchi (Ref. 39) observed that the arc column becomes narrower and brighter at high pressures and more diffused and rounded at low pressures. Yamamoto and Shimada (Refs. 3, 40) observed that the arc pressure at 32-mm Hg reached about one-tenth of that at atmospheric pressure. Based on these observations, the effective arc radius for current and heat distribution at 32-mm Hg pressure were assumed to be 10% more than their values at the atmospheric pressure. The effective arc radius is required for both heat transfer and fluid flow calculations as well as the arc velocity estimation. The expressions used in the calculations of arc radius are presented in Table 4, and the properties of shielding gas are given in Table 5. For each combination of arc current and welding speed, values of liquid metal velocity in the weld pool, U_l , shielding gas velocity, U_g , density of liquid metal, ρ_l , density of shielding gas, ρ_g , depth of weld pool, h_l , shielding gas layer height, h_g , length of weld pool, L_p , and surface tension of liquid metal, γ , were substituted in Equations 16B–D to calculate the value of (B^2-4AC) . The calculated line in Fig. 11 represents zero value of the (B^2-4AC) . The region below this line has a positive value of (B^2-4AC) and is free of humping defects. At 32 mm of Hg ambient pressure, the shielding gas density is low, which leads to low drag force and

welds free of humping as shown in Fig. 11. A comparison of Figs. 4 and 11 shows that by reducing the ambient pressure, critical welding speed can be increased by more than 200%. The computed critical welding speed for humping showed good agreement with the corresponding experimental values reported by Yamamoto and Shimada (Ref. 3) indicating accuracy of the model.

Effect of Torch Angle

To capture the effect of the torch angle (inclination) in the model, the effective arc length was modified by assuming an asymmetric weld pool surface shown in Fig. 12A, B. Since the front of the weld pool is depressed significantly more than the trailing region (Ref. 41), the trailing region is assumed to make a 45-deg angle with the horizontal plane along the welding direction as shown in Fig. 12. Based on the above assumption, the effective arc length was calculated using the geometry of the system shown in Fig. 12A for different torch angles. For inclined torch practice, the torch can have two orientations, pull and push, as shown in Fig. 12. A drag or pull technique provides more penetration and a narrower bead compared to a push technique where the arc is directed ahead of the weld bead. For the push configuration, $\phi > 0$, and the effective arc length was calculated using the following expression:

$$l_{eff} = \left(\frac{l_a + 0.5 \times \text{depth of weld pool}}{\cos(\phi)} \right) \quad \text{for } \phi \geq 0 \quad (29)$$

The presence of cosine of the inclination angle in the denominator increases the arc length and the arc radius on the weld pool surface. With increase in arc radius, the peak heat intensity decreases, which leads to a wider and shallower pool. The effective arc length for the pull technique when the arc was directed behind the weld bead, i.e., for $\phi < 0$, was calculated based on the geometry. The effective arc length for the pull technique (i.e., negative ϕ) shown in Fig. 12B was calculated from the following expression:

$$l_{eff} = \frac{l_a}{\cos(\phi)} + 0.5 \left(\frac{\sin(\pi/4) \times \text{depth of weld pool} - l_a \tan(\phi)}{\sin(\phi + \pi/4)} \right) \quad \text{for } \phi < 0 \quad (30)$$

Figure 13 shows the variation of weld pool depth with torch inclination angle,

ϕ . A reasonable agreement with the experimental results for different torch angles (Ref. 42) suggested that the above expressions of effective arc length could be used in the model. The depth and length of the weld pool was larger during the pull technique compared to the push technique for similar welding conditions. The calculations were done using a three-dimensional heat transfer and fluid flow model with modification for the electromagnetic force calculation (Refs. 28, 42) at different torch angles. This behavior matched very well with the effect of inclination of torch observed experimentally (Ref. 41). Figure 14 shows that the critical welding speed for humping defects increases with inclination of arc ahead of weld bead, i.e., during the push technique. For a 25-deg inclination, the computed critical welding speed increased by about 60%. This behavior was due to the decrease in both arc velocity and arc pressure on the weld pool surface with increase in the effective arc length. The inclination of torch in the negative direction (i.e., in pull or drag technique) reduced the critical welding speed and generated humping even at a lower speed as shown in Fig. 14A. Recently, Nguyen et al. (Ref. 43) observed that the critical welding speed during gas metal arc welding in spray mode increases when the gun is directed ahead of the weld bead. Lancaster (Ref. 25) also recommended the use of the welding torch in the push position to avoid humping. The computed results also showed a similar behavior.

Yamamoto and Shimada (Ref. 3) also showed the effect of the inclination of the torch on the critical welding speed at low ambient pressure. They found that at low ambient pressure, the inclination of the torch in the push direction increased the critical welding speed and vice versa. The computed critical welding speed, shown in Fig. 14B, for different torch inclination angles and 32-mm Hg ambient pressure, showed good agreement with the corresponding experimental values reported by Yamamoto and Shimada (Ref. 3) indicating the accuracy of the calculations.

Conclusions

A phenomenological model based on the stability of waves on the weld pool surface due to relative motion between the plasma and the liquid weld metal was developed to examine the conditions for the formation of humping defects. Good agreement was obtained between the model predictions for humping and independent experimental results from various sources for a wide variety of welding

conditions. This model can estimate the critical welding conditions for humping considering the values of arc current, welding speed, nature of the shielding gas, electrode geometry, ambient pressure, torch angle, and external magnetic field during gas tungsten arc (GTA) welding. The following conclusions can be drawn from the results.

- 1) Increase in welding speed above certain critical speed leads to initiation of humping defects.
- 2) The value of the critical speed varies with the welding conditions. The critical welding speed decreases with increase in arc current.
- 3) The nature of the shielding gas affects humping. Chances of humping are lower in He than in Ar.
- 4) Blunt electrodes with large tip angles help in preventing humping.
- 5) Application of external magnetic field in transverse direction that deflects arc in the welding direction helps in avoiding humping.
- 6) Low ambient pressure reduces the occurrence of humping.
- 7) The inclination of the torch away from the welding direction, i.e., in push position, suppresses humping while the torch in pull position favors humping.

These results show that the adjustment of welding variables can prevent humping. Even when high welding speed and current are needed to sustain productivity goals, several steps can be taken to prevent humping. These include selection of hollow electrodes, imposition of appropriate external magnetic field, inclination of the torch, careful selection of shielding gas and, where practical, reduced pressure.

Acknowledgments

This research was supported by a grant from the U.S. Department of Energy, Basic Energy Sciences, Division of Materials Sciences, under grant number DE-FGO2-01ER45900. Amit Kumar gratefully acknowledges award of a Fellowship from the American Welding Society.

Appendix A: Derivation of Kelvin-Helmholtz Instability Model

The pressure difference along the interface was calculated by considering the force balance in a direction perpendicular to arc segment PQ of length ds shown in Fig. 2, as follows (Refs. 10–12):

$$-P_g ds + P_1 ds + \gamma d\theta = 0$$

where γ is the surface tension of the liquid metal in the weld pool and $d\theta$ is the

included angle between the tangential forces acting on arc segment PQ. Furthermore, the pressure difference is related to the radius of curvature, r , by the following relation (Refs. 10–12):

$$P_g - P_1 = \gamma \frac{d\theta}{ds} = \frac{\gamma}{r} \quad (A1)$$

The curvature $1/r$ of the surface wave profile, η , is given by (Refs. 10–12)

$$\frac{1}{r} = \frac{\partial^2 \eta / \partial x^2}{\left[1 + \left(\partial \eta / \partial x\right)^2\right]^{3/2}} \approx \frac{\partial^2 \eta}{\partial x^2} \quad (A2)$$

Equation A2, valid for small slopes, can be substituted in Equation A1 to obtain the following equation:

$$P_g - P_1 = \gamma \frac{\partial^2 \eta}{\partial x^2} \quad (A3)$$

After subtracting Equation 13A from Equation 13B and neglecting the nonlinear velocity terms, for small amplitude waves, we get

$$\begin{aligned} P_g - P_1 + \rho_g \left[\frac{\partial \Phi_g}{\partial t} + g\eta \right] \\ - \rho_1 \left[\frac{\partial \Phi_1}{\partial t} + g\eta \right] = 0 \end{aligned}$$

After substituting the value of pressure difference at the interface (i.e., Equation A3) in the above expression, we get

$$\begin{aligned} \gamma \frac{\partial^2 \eta}{\partial x^2} + \rho_g \left[\frac{\partial \Phi_g}{\partial t} + g\eta \right] \\ - \rho_1 \left[\frac{\partial \Phi_1}{\partial t} + g\eta \right] = 0 \quad (A4) \end{aligned}$$

For the lower liquid metal layer and the upper gaseous layers, the velocity potentials, Φ_1 and Φ_g , which satisfy the Equations 8A, 8B, 9A, 9B, 12A, and 12B can be written as

$$\begin{aligned} \Phi_1 = U_1 x \\ + B_1 e^{ik(x-\alpha)} \cosh \left[k(z+h_1) \right] \quad (A5a) \end{aligned}$$

$$\begin{aligned} \Phi_g = U_g x \\ + B_2 e^{ik(x-\alpha)} \cosh \left[k(z-h_g) \right] \quad (A5b) \end{aligned}$$

where B_1 and B_2 are constants whose value will be calculated based on the remaining boundary conditions given by Equations 10A, 10B, and A4. After substituting the values of velocity potentials,

Φ_1 , Φ_g , and η from Equations A5a, A5b, and 5 in Equations 10A and 10B and rearranging the terms, we get (Refs. 10, 12)

$$B_1 = -\frac{iak(c-U_1)\alpha s \alpha (h_i k)}{k} \quad (A6a)$$

$$B_2 = \frac{ika(c-U_g)\alpha s \alpha (h_g k)}{k} \quad (A6b)$$

After substituting the values of Φ_1 , Φ_g , and η in Equation A4, we get

$$\begin{aligned} e^{ik(x-ct)}\gamma ak^2 - \rho_1(iB_1 ce^{ik(x-ct)}k \cosh(k(h_1+z)) \\ - iB_1 e^{ik(x-ct)}k U_1 \cosh(k(h_1+z)) - e^{ik(x-ct)}ga) \\ + \rho_g(iB_2 ce^{ik(x-ct)}k \cosh(k(z-h_g)) \\ - iB_2 e^{ik(x-ct)}k U_g \cosh(k(z-h_g)) \\ - e^{ik(x-ct)}ga) = 0 \end{aligned} \quad (A7)$$

Dividing Equation A7 by the term $e^{ik(x-ct)}$ and putting $z = 0$ at the interface, we get

$$\begin{aligned} \gamma ak^2 - \rho_1(iB_1 ck \cosh(kh_1) \\ - iB_1 k U_1 \cosh(kh_1) - ga) \\ + \rho_g(iB_2 ck \cosh(kh_g) \\ - iB_2 k U_g \cosh(kh_g) - ga) = 0 \end{aligned} \quad (A8)$$

Substituting the values of B_1 and B_2 in Equation A8 and rearranging the terms:

$$(A9)$$

After canceling the amplitude 'a' from all the terms in Equation A9, we get the following dispersion relation for wave speed.

$$\begin{aligned} k\rho_1(U_1-c)^2 \coth(h_1 k) \\ + k\rho_g(U_g-c)^2 \coth(h_g k) \\ = \gamma k^2 + g(\rho_1 - \rho_g) \end{aligned} \quad (A10)$$

Equation A10 describes the dependency of various variables on surface wave velocity.

Appendix B: Heat Transfer and Fluid Flow Model

The flow of liquid metal in the weld pool in a three-dimensional Cartesian coordinate system is represented by the following momentum conservation equation (Refs. 13–21):

$$\begin{aligned} \rho \frac{\partial u_j}{\partial t} + \rho \frac{\partial (u_i u_j)}{\partial x_i} \\ = \frac{\partial}{\partial x_i} \left(\mu \frac{\partial u_j}{\partial x_i} \right) + S_j \end{aligned} \quad (B1)$$

where ρ is density of the metal, x_i is the distance along the $i = 1, 2,$ and 3 directions, u_j is the velocity component along the j direction, μ is the viscosity of the liquid metal, and S_j is the source term for the j^{th} momentum equation and is given as (Refs. 13–21):

$$\begin{aligned} S_j = -\frac{\partial p}{\partial x_j} + \frac{\partial}{\partial x_i} \left(\mu \frac{\partial u_i}{\partial x_j} \right) - C \left(\frac{(1-f_L)^2}{f_L^3 + B} \right) u_j \\ + \rho g \beta (T - T_{ref}) - \rho U \frac{\partial u_j}{\partial x_1} + S_{b_j} \end{aligned} \quad (B2)$$

where p is the pressure, f_L is the liquid fraction, B is a constant introduced to avoid division by zero, $C (=1.6 \times 10^4)$ is a constant that takes into account mushy zone morphology, g is acceleration due to gravity, β is thermal expansion coefficient, T_{ref} is the reference ambient temperature, U is the welding speed along direction 1, and S_{b_j} represents the electromagnetic source term (Refs. 13, 14, 28). The third term on the right-hand side (RHS) represents the frictional dissipation in the mushy zone according to the Carman-Kozeny equation for flow through a porous media (Refs. 44, 45). The pressure field was obtained by solving the following continuity equation simultaneously with the momentum equation:

$$\frac{\partial (\rho u_i)}{\partial x_i} = 0 \quad (B3)$$

The total enthalpy H is represented by a sum of sensible heat h and latent heat content ΔH , i.e., $H = h + \Delta H$ where $h = \int C_p dT$, $\Delta H = f_L L$, and C_p is the specific heat of the liquid metal. The liquid fraction f_L is assumed to vary linearly with temperature in the mushy zone (Refs. 13–21):

where T is the temperature, T_L is liquidus temperature, and T_S is the solidus temperature. The thermal energy transport in the weld workpiece can be expressed by the following modified energy equation (Refs. 13–21):

$$f_L = \begin{cases} 1 & T > T_L \\ \frac{T - T_S}{T_L - T_S} & T_S \leq T \leq T_L \\ 0 & T < T_S \end{cases} \quad (B4)$$

$$\begin{aligned} \rho \frac{\partial h}{\partial t} + \rho \frac{\partial (u_i h)}{\partial x_i} = \frac{\partial}{\partial x_i} \left(\frac{k}{C_p} \frac{\partial h}{\partial x_i} \right) \\ - \rho \frac{\partial (\Delta H)}{\partial t} - \rho \frac{\partial (u_i \Delta H)}{\partial x_i} - \rho \frac{\partial (U \Delta H)}{\partial x_i} \\ - \rho \frac{\partial (U h)}{\partial x_i} \end{aligned} \quad (B5)$$

Since the weld is symmetrical about the weld centerline only half of the workpiece is considered. The weld top surface is assumed to be flat. The velocity boundary condition is given as (Refs. 13–21)

$$\begin{aligned} \mu \frac{\partial u}{\partial z} = f_L \frac{d\gamma}{dT} \frac{\partial T}{\partial x} \\ \mu \frac{\partial v}{\partial z} = f_L \frac{d\gamma}{dT} \frac{\partial T}{\partial y} \\ w = 0 \end{aligned} \quad (B6)$$

where $d\gamma/dT$ is temperature coefficient of surface tension and $u, v,$ and w are the velocity components along the $x, y,$ and z directions, respectively. As shown in this equation, the u and v velocities are determined from the Marangoni effect. The w velocity is equal to zero since there is no flow of liquid metal perpendicular to the pool top surface. The heat flux at the top surface is given as (Ref. 42)

$$\begin{aligned} k \frac{\partial T}{\partial z} = \frac{dQ\eta}{\pi r_b^2} \exp \left(-d \left[\frac{x^2}{r_b^2 \cos^2 \phi} + \frac{y^2}{r_b^2} \right] \right) \\ - \sigma \epsilon (T^4 - T_a^4) - h_c (T - T_a) \end{aligned} \quad (B7)$$

where k is thermal conductivity, d is the energy distribution factor, Q is total arc power, η is the arc efficiency, r_b is the effective arc radius, ϕ is torch inclination angle, σ is Stefan-Boltzmann constant, ϵ is the emissivity, T_a is ambient temperature, and h_c is the convective heat transfer coefficient. The first term on the right-hand side is the heat input from the heat source, defined by an ellipsoidal Gaussian heat distribution (Ref. 42). For zero torch inclination angle, the ellipsoidal Gaussian heat distribution becomes the same as the symmetric circular Gaussian heat distribution. The second and third terms represent the heat loss by radiation and convection, respectively. The boundary conditions are defined as zero flux across the symmetric surface as

$$\frac{\partial u}{\partial y} = 0, v = 0, \frac{\partial w}{\partial y} = 0 \quad (B8)$$

$$\frac{\partial h}{\partial y} = 0 \quad (\text{B9})$$

At all other surfaces, temperatures are set at ambient temperature and the velocities are set to be zero. The electromagnetic source term in Equation B2 was calculated using the modified electromagnetic force model (Refs. 28, 42), which can calculate the electromagnetic force for any current density distribution.

References

- Bradstreet, B. J. 1968. Effect of surface tension and metal flow on weld bead formation. *Welding Journal* 47(7): 314-s to 322-s.
- Savage, W. F., Nippes, E. F., and Agusa, K. 1979. Effect of arc force on defect formation in GTA welding. *Welding Journal* 58(7): 212-s to 224-s.
- Yamamoto, T., and Shimada, W. 1975. A study on bead formation in high speed TIG arc welding. *International Symposium in Welding*, Osaka, Japan.
- Beck, M., Berger, P., Dausinger, F., and Hugel, H. 1991. Aspects of keyhole/melt interaction in high speed laser welding. *Proceedings of 8th International Symposium on Gas Flow and Chemical Lasers*, Madrid, Spain.
- Mills, K. C., and Keene, B. J. 1990. Factors affecting variable weld penetration. *International Materials Reviews* 35(4): 185–216.
- Gratzke, U., Kapadia, P. D., Dowden, J., Kroos, J., and Simon, G. 1992. Theoretical approach to the humping phenomenon in welding processes. *Journal of Physics D: Applied Physics* 25: 1640–1647.
- Yamauchi, N., and Taka, T. 1978. Bead formation in TIG welding. *International Institute of Welding*, document no.: 212-437-78.
- Mendez, P. F., and Eagar, T. W. 2003. Penetration and defect formation in high-current arc welding. *Welding Journal* 82(10): 296-s to 306-s.
- Mendez, P. F., Niece, K. L., and Eagar, T. W. 2000. Humping formation in high current GTA welding. *Proceedings of the International Conference on Joining of Advanced and Specialty Materials II, Materials Solutions '99*, Cincinnati, Ohio, pp 151–158.
- Kundu, P. K., and Cohen, I. M. 2004. *Fluid Mechanics*. San Diego, Calif.: Elsevier Academic Press. pp 2004–235.
- Thomson, L. M. 1968. *Theoretical Hydrodynamics*. New York, N.Y.: Macmillan. pp 426–464.
- Drazin, P. G., and Reid, W. H. 2004. *Hydrodynamic Stability*. Cambridge, UK: University Press. pp 8–31.
- Mundra, K., DebRoy, T., and Kelkar, K. M. 1996. Numerical prediction of fluid flow and heat transfer in welding with a moving heat source. *Numerical Heat Transfer A* 29: 115–129.
- Zhang, W., Roy, G. G., Elmer, J. W., and DebRoy, T. 2003. Modeling of heat transfer and fluid flow during gas tungsten arc spot welding of low carbon steel. *Journal of Applied Physics* 93(5): 3022–3033.
- De, A., and DebRoy, T. 2004. A smart model to estimate effective thermal conductivity and viscosity in weld pool. *Journal of Applied Physics* 95(9): 5230–5239.
- De, A., and DebRoy, T. 2004. Probing unknown welding parameters from convective heat transfer calculation and multivariable optimization. *Journal of Physics D: Applied Physics* 37: 140–150.
- De, A., and DebRoy, T. 2005. Reliable calculations of heat and fluid flow during conduction mode laser welding through optimization of uncertain parameters. *Welding Journal* 84(7): 101–112.
- Mishra, S., and DebRoy, T. 2005. A computational procedure for finding multiple solutions of convective heat transfer equation. *Journal of Physics D* 38: 2977–2985.
- Mishra, S., and DebRoy, T. 2005. A heat transfer and fluid flow based model to obtain a specific weld geometry through multiple paths. *Journal of Applied Physics* 98(4): Article No. 044902.
- He, X., Fuerschbach, P., and DebRoy, T. 2003. Heat transfer and fluid flow during laser spot welding of 304 stainless steel. *Journal of Physics D: Applied Physics* 36: 1388–1398.
- Mundra, K., Blackburn, J. M., and DebRoy, T. 1997. Absorption and transport of hydrogen during GMA welding of mild steels. *Science and Technology of Welding and Joining* 2: 174–184.
- Chang, C. W., Eagar, T. W., and Szekely, J. 1980. The modeling of gas velocity fields in welding arc. *Arc Physics and Weld Pool Behavior*, The Welding Institute, Cambridge, England, pp 381–388.
- Patankar, S. V. 1982. *Numerical Heat Transfer and Fluid Flow*. New York, N.Y.: McGraw-Hill. pp 41–71.
- Sahoo, P., DebRoy, T., and McNallan, M. J. 1988. Surface tension of binary metal-surface active solute systems under conditions relevant to welding metallurgy. *Metallurgical Transaction B* 19B: 483–491.
- Lancaster, J. F. 1986. *The Physics of the Welding*. Oxford, UK: Pergamon. pp 120–225.
- Goldman, K. 1966. Electric arcs in argon. *Physics of the Welding Arc*. London, UK: Institute of Welding.
- Lin, M. L., and Eagar, T. W. 1985. Influence of arc pressure on weld pool geometry. *Welding Journal* 64(6): 163-s to 169-s.
- Kumar, A., and DebRoy, T. 2003. Calculation of three-dimensional electromagnetic force field during arc welding. *Journal of Applied Physics* 94 (2): 1267–1277.
- Kou, S., and Sun, D. K. 1985. Fluid flow and weld penetration in stationary arc welds. *Metallurgical Transactions A* 16A: 203–213.
- Rokhlin, S. I., and Guu, A. C. 1993. A study of arc force, pool depression and weld penetration during gas tungsten arc welding. *Welding Journal* 72(8): 381–390.
- Tsai, N. S., and Eagar, T. W. 1985. Distribution of arc and current fluxes in gas tungsten arcs. *Metallurgical Transactions B* 16(12): 841–846.
- Yamauchi, N., and Taka, T. 1979. TIG arc welding with a hollow tungsten electrode. *International Institute of Welding*, document no.: 212-452-79.
- Mondain-Monval. 1973. The physical properties of fluids at elevated temperatures. *IIW document* 212-264-73.
- Goodarzi, M., Choo, R., and Toguri, J. M. 1997. The effect of the cathode tip angle on the GTAW arc and weld pool: I. Mathematical model of the arc. *Journal of Physics D: Applied Physics* 30: 2744–2756.
- Choo, R. T. C., Szekeley, J., and Westhoff, R. C. 1990. Modelling of high current arcs in welding with emphasis on free surface phenomena in weld pool. *Welding Journal* 69(9): 346-s to 361-s.
- Chernyshov, G. G., and Kovtun, V. L. 1985. Effect of heat flow and arc pressure on maximum welding speed. *Welding Production* 32(2): 23–25.
- Kang, Y. H., and Na, S. J. 2002. A study on the modeling of magnetic arc deflection and dynamic analysis of arc sensor. *Welding Journal* 81(1): 8–13.
- Kovalev, I. M. 1965. Deflection of a welding arc in a transverse magnetic field. *Welding Production* 12(10): 9–14.
- Matsunawa, A., and Nishiguchi, K. 1979. Arc characteristics in high pressure argon atmospheres. *Arc Physics and Weld Pool Behavior*. The Welding Institute, Cambridge, UK.
- Yamamoto, T., and Shimada, W. 1968. Cathode zone and its effect on the penetration of the TIG arc at low pressure atmosphere. *International Institute of Welding*, document no.: 212-157-68.
- Welding Handbook*. 2004. Miami, Fla.: American Welding Society.
- Fan, Y. 2003. The effect of torch angle on fluid flow and heat transfer during GTA welding. M.S. thesis, The Pennsylvania State University, Pa.
- Nguyen, T. C., Weckman, D. C., Johnson, D. A., and Kerr, H. W. 2005. The humping phenomenon during high speed gas metal arc welding. *Science and Technology of Welding and Joining* 10(4): 447–459.
- Voller, V. R., and Prakash, C. 1987. A fixed grid numerical modeling methodology for convection diffusion mushy region phase change problems. *International Journal of Heat and Mass Transfer* 30(8): 1709–1719.
- Brent, A. D., Voller, V. R., and Reid, K. J. 1988. Enthalpy-porosity technique for modeling convection-diffusion phase change – Application to the modeling of a pure metal. *Numerical Heat Transfer* 13: 297–318.